

Decrystallization of CH₃NH₃PbI₃ perovskite crystals via polarity dependent localized charges

Min-cheol Kim^{a†}, Namyoung Ahn^{a†}, Eunhak Lim^b, Young Un Jin^c, Peter V. Pikhitsa^a, Jiyoung Heo^d, Seong Keun Kim^b, Hyun Suk Jung^{c} and Mansoo Choi^{a,e*}*

^aGlobal Frontier Center for Multiscale Energy Systems, Seoul National University, Seoul, Republic of Korea.

^bDepartment of Chemistry, Seoul National University, Seoul, Republic of Korea.

^cSchool of Advanced Materials Science & Engineering, Sungkyunkwan University, Suwon, Gyeonggi-do, Republic of Korea.

^dDepartment of Green Chemical Engineering, Sangmyung University, Seoul, Republic of Korea.

^eDepartment of Mechanical Engineering, Seoul National University, Seoul, Republic of Korea.

[†]These authors contributed equally to this work.

*Correspondence and request for materials should be addressed to H.S.J, and M. C.

(email: hsjung1@skku.edu; mchoi@snu.ac.kr)

Abstract

Despite soaring performance of organic-inorganic hybrid perovskite materials in recent years, the mechanism of their decomposition at actual operation condition has been elusive. Herein, we elucidated the decrystallization process of $\text{CH}_3\text{NH}_3\text{PbI}_3$ perovskite crystals via localized charges and identified polarity-dependent degradation pathway by carrying out time-evolution measurements for absorption spectra of perovskite films with underlying different charge transport layers and *ab initio* molecular dynamics calculations. It was found that the carrier polarity (hole-rich or electron-rich) inside the perovskite films played a critical role in the degradation rate, and polarity-dependent degradation pathway strongly depended on the combination of surrounding gaseous molecules. The hole-rich perovskite films degraded more rapidly in the existence of H_2O than the electron-rich one, while the degradation trend became opposite in only-oxygen ambient. Strikingly, the hole-rich one was extremely weak to atmospheric air containing both H_2O and O_2 , whereas the MAPbI_3 film with excessive electrons rather stabilized in air. *Ab initio* molecular dynamics (AIMD) simulation was also done to find the detailed degradation pathway of MAPbI_3 under atmosphere for different polarity of localized charge, which are in good agreement with experimental results. Furthermore, X-ray assisted spectroscopic measurements confirmed the production of Pb(OH)I as predicted from the simulation result.

Perovskite is an ionic crystal with three kinds of ions, in which the cation and anion are being held together by electrostatic forces. As one of perovskite materials, organic-inorganic hybrid perovskites have currently attracted worldwide attention due to their excellent performance for photovoltaics,¹⁻⁴ but those have shown unstable characteristics against light and air.^{5, 6} Since such hybrid perovskites have weaker hydrogen bonding between organic cation and octahedral structure than inorganic ones,⁷ organic cations have been considered to be responsible for easy crystal de-bonding and chemical reaction with atmosphere.^{8, 9} Hybrid perovskites rapidly change into inorganic halide after light-induced degradation.¹⁰ Such fast decomposition of hybrid perovskites impedes to commercialize perovskite-based photovoltaics.

Degradation of these perovskite materials have been studied for past few years,¹¹⁻¹⁴ however, there remain a lot of unknowns and debates on degradation mechanism because the process happens under extremely complicated multi-molecular systems in real operation condition.^{10, 15, 16} As possible causes, researchers previously suggested that ion migration of halide anion and resulting deprotonation of organic cation.^{5, 11, 17, 18} However, it is possible that observed ion migration and deprotonation could be merely a result of degradation, not the origin of degradation. Accordingly, digging out the fundamental reason of degradation is highly urgent to solve the stability issue.

Our group had pointed out trapped charges in perovskite ionic crystals as the fundamental origin.^{19, 20} We experimentally demonstrated that trapped-charges along grain boundaries and also on grain surfaces induced irreversible degradation in the presence of water, oxygen or air. We also carried out *ab initio* molecular dynamics (AIMD) simulation for $\text{CH}_3\text{NH}_3\text{PbI}_3$ (MAPbI₃) crystals with adsorbates of either H₂O and O₂ to examine whether the trapped charges could trigger the degradation of the MAPbI₃. From these experiments and simulations, we uncovered atomistic mechanism for trapped-charge driven degradation of

MAPbI₃, in which trapped-charges play a decisive role in breaking MAPbI₃ lattices as a consequence of intermolecular interaction with gaseous molecules under light soaking. However, it still remains unknown whether the polarity of trapped charges could result in different pathways of the degradation of perovskite materials under the interaction with multi-molecular species in the real operation condition.

In the present work, we found a strong evidence to support our trapped-charge driven degradation and identified its polarity dependent decrystallization process through light-induced degradation test of MAPbI₃ perovskite films coated on different charge-selective layers.^{21, 22} The hole- and electron-rich MAPbI₃ layer can be realized in half devices which were fabricated by coating selective charge transporting underlying layers. The existence of unbalanced hole and electron densities was evidenced by photoluminescence (PL), Kelvin force microscopy (KPFM) measurements and theoretical calculations. These electron or hole-rich half devices were exposed to different gaseous molecules to dig into the role of polarity dependent localized charges on the degradation. In moisture-only ambient, the degradation rate of the hole-rich MAPbI₃ film was faster than that of electron-rich one, while oxygen-only case presented totally-inverted results with respect to the degradation rates. More importantly, the actual atmospheric conditions (when oxygen and moisture exist together) were highly aggressive only for the hole-rich MAPbI₃ film, whereas the electron-rich one rather stabilized (even more stable than oxygen-only case). Such interesting results suggest that there exists a direct correlation between polarity dependent localized charges and degradation. To explain why and how charge polarity influences the degradation rates depending on environments, we conducted AIMD simulations to study intermolecular interactions between MAPbI₃ components and mixture gas (oxygen and water) with different charge state (charge polarity of MAPbI₃). In the simulations, under the mixture of oxygen and water, it was found in the hole-

rich case (with positive charge) that strong interaction of Pb-O bonding induces the vigorous destruction of PbI_6 octahedron and finally generates hydroxide species are formed as a consequence of proton transfer from H_2O , which was experimentally confirmed from X-ray assisted spectroscopic measurements in the present study.

Results

Different degradation rates of MAPbI₃ depending on underlying transport layers

We employed perovskite films with different underlying layers to investigate the effect of underlying layers on degradation rates under light illumination in the same ambient condition. We configured the half device with ITO/selective charge extraction layer/MAPbI₃, in which surfaces of MAPbI₃ films were directly exposed to air without any passivation layer, and this configuration enables films to be exposed to the same ambient condition under light illumination. As we will discuss in detail later, half devices have unbalanced polarity of charge carriers inside the MAPbI₃ films (due to selective charge extraction and consequently cause unbalanced surface localized charges confirmed by SKPM.²³) We carried out degradation tests with different ambient conditions by using our customized experimental setup that can keep specific ambient condition inside the chamber. (**Fig. 1a**) Interestingly, the degradation of the PEDOT:PSS/MAPbI₃ half device which has excessive electrons happened much faster than that of the C₆₀/MAPbI₃ half device which has excessive holes in dry air ambient (N₂(80%)+O₂(20%)) (**Fig. 1b, c**), while humidified nitrogen ambient (N₂+H₂O R.H.~80%) caused totally inverted results, i.e. in this case, C₆₀/MAPbI₃ half device containing excessive holes degraded much faster than the case of PEDOT:PSS/MAPbI₃ (**Fig. 1d, e**). Under 100% oxygen ambient condition, the degradation occurred more rapidly than dry air ambient, but exhibited the same trend depending on the underlying layers (**Supplementary Fig. 1**). It is noteworthy that the PEDOT:PSS/MAPbI₃ half device shows very slow degradation in the humidified nitrogen ambient in contrast to the C₆₀/MAPbI₃ half device. When surrounded only by nitrogen, no light-induced degradation of the MAPbI₃ film was observed regardless of the underlying transport layers (**Supplementary Fig. 2**), which is consistent with previous studies.^{5, 19} This means that the underlying transport layers themselves cannot deteriorate the

MAPbI₃ films even with unbalanced localized charges.

Previously, it was found that MAPbI₃ films were decomposed under light illumination in dry air ambient even without moisture.^{5, 11} This study demonstrated that superoxide (O₂⁻) formed by the reaction of oxygen molecules with photo-generated electron could degrade MAPbI₃ perovskites without water molecules. The authors claimed that, in the case of the TiO₂/MAPbI₃ half device which can selectively quench electrons, superoxide generation decreased as compared to the case of either the glass/MAPbI₃ or Al₂O₃/MAPbI₃ half device, which finally led to relatively slow degradation. Our experimental results also present similar results in dry air ambient (**Fig. 1b, c**). However, the degradation rate in humidified nitrogen ambient was completely reversed, which has not been known before. These observations clearly show strong dependency of degradation rate on the kind of underlying layers and surrounding ambient conditions. Obviously, different charge transport layer changes the distribution of charge carrier polarity inside the MAPbI₃ layer.

Unbalanced charge carrier polarity inside MAPbI₃ layers

To explain such interesting phenomena, it is required to analyze how the kind of underlying layers leads to difference in degradation rates. The kind of underlying layers influence carrier density distributions in the MAPbI₃ layer under light illumination.²³ We prepared four different half devices to examine the change in carrier densities depending on the underlying layers via photoluminescence (PL) measurements. We used C₆₀²⁴ and PC₆₀BM²⁵ as ETLs, and PEDOT:PSS²⁶ and Spiro-MeOTAD²⁷ as HTLs for half device configurations. Since radiative recombination is proportional to electron and hole densities,²⁸ PL intensities are indicative of carrier densities in MAPbI₃ layers. Dramatic decreases in PL intensities were observed with the case of either electron transport layer (ETL)/MAPbI₃ or hole transport layer (HTL)/MAPbI₃

half devices compared to the case without transport layers, which indicates that photo-generated electrons and holes are selectively collected at the interface, respectively (**Supplementary Fig. 3**). In the Spiro-MeOTAD case, additives such as TBP and Li-TFSI were not added to avoid of controversial issue on the effect of their corrosive properties.^{29, 30} Its charge extraction property was not significantly influenced by the absence of additives, as indicated by the results of PL measurements (**Supplementary Fig. 4**). In the same manner, time-resolved PL data also presented strong carrier extraction properties of ETL/MAPbI₃ and HTL/MAPbI₃ half devices (**Supplementary Fig. 3**). The values of τ_1 (the fastest decay component) for these half devices, which correspond to charge injection,³¹ were far smaller than that for the glass/MAPbI₃ film as can be seen in Supplementary Table 1. In other words, these results imply that such charge-selective layers strongly attract a particular carrier from MAPbI₃ films at the interfaces.

Based on PL results, we can assume that electron and hole density at the interface is zero in the case of ETL/MAPbI₃ and HTL/MAPbI₃ device, respectively. By solving carrier continuity equation considering light absorption, carrier mobility, carrier recombination, carrier drift and diffusion, we calculated electron and hole densities as a function of thickness displacement under one sun illumination for different underlying layers. (**Calculation details in Supplementary Information**). **Fig. 2c-e** show calculation results of electron (n_e , indicated in red line) and hole (n_h , indicated in blue line) density distributions depending on different underlying layers. The glass/MAPbI₃ device have uniform distributions due to the absence of the charge selection layer, in which the orders of magnitude in hole and electron density are similar. Small difference originates from mobility difference between electron and hole.³² On the other hand, in the ETL/MAPbI₃ device, hole densities are much higher than electron densities due to electron quench at the ETL interface. Strong and fast electron transfer from MAPbI₃ to ETL is inferred from a steep slope of electron densities near the ETL interface.

Instead, the HTL/MAPbI₃ device have inverted carrier distributions. It is also confirmed not only that hole densities dramatically change near the HTL interface like the ETL/MAPbI₃ case, but also that electron density is higher than hole density. It is clearly shown that the kind of underlying layer results in the unbalance of carrier polarity inside MAPbI₃ film when photo-carriers are generated by light illumination. Additionally, we performed Kelvin probe force microscopy (KPFM) measurements to experimentally demonstrate unbalance of charge carrier.³³ Imbalance carrier concentration inside the MAPbI₃ layer can alter quasi fermi level as depicted in **Supplementary Fig. 5**, which correspondingly could change surface potential. **Fig. 2f-h** clearly show different surface potentials depending on the underlying layer, which is in good agreement with density distribution calculations. Since hole densities are much higher than electron densities in the ETL/MAPbI₃ half device regardless of thickness displacement, the device shows the highest potentials among three kinds of half devices (**Fig. 2i**). Based on the trapped charge driven degradation mechanism¹⁹, we can hypothesize that the different degradation phenomena for different charge selective layers would be attributed to different charge polarity (electron-rich or hole-rich) inside the MAPbI₃ films.

Correlation between degradation rates and charge polarity under different ambient conditions

Since we investigated the light-induced degradation of half device configurations under the oxygen-only or humidified nitrogen-only condition so far, we additionally performed the degradation experiments under atmospheric air condition containing both oxygen and water. (see **Fig. 3a, b** and **Supplementary Fig. 6**.) We observed unexpected outcomes from these experiments in terms of degradation rates. The complete deterioration of the ETL/MAPbI₃ device took place within 12 hours as shown in **Fig. 3a**. The degradation rates were by far faster

than those under either dry air or humidified nitrogen ambient (see **Fig. 3c**). Namely, the mixture of oxygen and water violently destroyed the ETL/MAPbI₃ devices, as compared to the case of only-oxygen or only-water ambient. On the other hand, the HTL/MAPbI₃ devices showed surprisingly enhanced stability under humidified air as seen in **Fig. 3b**. The remarkable point of observations in case of HTL/MAPbI₃ is the fact that the degradation under air with moisture occurred more slowly than the degradation either under air without moisture or humidified nitrogen without oxygen (**Fig. 3d**). Surprisingly, an addition of moisture rather improved the stability of the HTL/MAPbI₃ device. Consequently, the mixture of oxygen and water gives rise to extremely diametrical effects on degradation rate depending on the kind of underlying layers (different excessive carrier polarity). The origin of such different degradation rate is further studied in atomic scale by AIMD simulation discussed below.

The X-ray diffraction (XRD) patterns obtained for the pristine and illuminated MAPbI₃ films deposited on different charge transport layers supports the observation (**Supplementary Fig. 7**). The MAPbI₃ films with localized hole were characterized by the stronger intensities of their PbI₂ (100) peaks as compared to those with localized electron samples, which was in good agreement with the results of absorption studies. The observed change in the PbI₂ (100)/MAPbI₃ (110) peak intensity ratio before and after illumination is summarized in **Supplementary Table 2**. The obtained scanning electron microscopy (SEM) images demonstrate the same light stability trends that were observed during the absorption and XRD studies (**Supplementary Fig. 8** and **Supplementary Fig. 9**). These results from optical, spectroscopic and morphological analysis indicate that gaseous molecules and their combination result in different degradation pathways depending on localized charge polarity of MAPbI₃ crystals.

We also investigated balanced charge carrier density case by testing MAPbI₃ film with

no transporting layer (glass/MAPbI₃). In the case, the light-induced degradation happened at a similar rate to the ETL/MAPbI₃ as shown in **Supplementary Fig. 6**. Even if the MAPbI₃ have balanced carrier densities of electrons and holes, the magnitude of carrier densities is much larger than those of the ETL or HTL/MAPbI₃ (**Fig. 2c-e**), which induced faster degradation than expected. Moreover, since MAPbI₃ crystals might have locally unbalanced carrier densities at defect sites such as grain boundaries,³⁴ high carrier densities of holes can cause such fast degradation of the glass/MAPbI₃ film under air conditions.

Discussion

Different degradation rates of MAPbI₃ under H₂O-only and O₂-only ambients

It is noteworthy that degradation rates of MAPbI₃ highly depend on charge carrier density and surrounding ambient. We have demonstrated trapped-charge driven degradation mechanism evidenced by experimental results and AIMD simulations in our previous works. As additional evidence for trapped-charge driven degradation, we newly discovered that unbalance of charge carrier (charge polarity) plays a different role in degradation rates in the present work. Based on AIMD simulation results in our previous work, we could find out how the charge polarity determine different degradation rates under H₂O-only and O₂-only ambient. According to simulation results, the H₂O-only ambient shows different solvation characteristics depending on the polarity of MAPbI₃ crystals.²⁰ Water molecules solvate methylammonium cation (MA⁺) at the surface of MAPbI₃ crystal with localized hole (positive polarity), while, in the case of negative polarity, water molecules surround and solvate iodide anion (I⁻). Since hydrogen bonding between MA⁺ and PbI₆⁻ is weaker than the covalent bonding of Pb and I in PbI₆ octahedron, MA⁺ could be more easily solvated by water due to such weak bond strength. As a result, MAPbI₃ crystals with localized hole became unstable in only-moisture case due to

easy solvation of MA^+ . Relatively heavy I^- anion with strong bonding is more durable against water solvation in the case of MAPbI_3 with negative polarity. These observations are in good agreement with our present experimental results regarding only-moisture degradation test (**Fig. 1d, e**). Next, in the only-oxygen case, MAPbI_3 crystals with negative polarity were broken down faster than ones with localized hole, which was attributed to highly reactive superoxide generation. In our previous AIMD simulation results,²⁰ generated-superoxide formed Pb-O bonding, thereby broke down PbI_6^- octahedral. The different quantity of generated superoxide depending on charge polarity was revealed from these simulation results. The MAPbI_3 crystals with negative polarity generate more superoxides than the positive case, which is consistent with the reference reported by Haque's group.^{5, 11} The difference of degradation rates from our experimental results under only-oxygen ambient (**Fig. 1b, c**) can be clearly explained by quantity difference of superoxide generation.

AIMD simulations for MAPbI_3 decrystallization under the mixture of O_2 and H_2O

We observed totally different degradation behavior in the presence of both oxygen and water (**Fig. 3a, b**), of which the reason is still elusive. Different synergetic effects of the combination of oxygen and water on degradation rate definitely indicate that there exist distinct and complicated intermolecular actions depending on charge polarity of MAPbI_3 crystals. Therefore, it is of high importance to investigate the mechanism of the degradation of MAPbI_3 at real operation condition containing both oxygen and water. In order to explore intermolecular dynamics of oxygen and water depending on the polarity of localized charges, AIMD simulations with configuration containing both oxygen and water molecules were performed for the first time. We set an initial geometry with 2 rigidly fixed MAPbI_3 units in the bottom, 2 relaxed MAPbI_3 units at the top to form the surface, and embed oxygen and water molecules

into gaps between atoms. The surface of MAPbI₃ crystals are terminated with MA cations and I anions and given different net charges (+1, 0, or -1) in the unit cell to model localized charges. **Fig. 4a-c** show molecular dynamics of MAPbI₃ crystals with surrounding one oxygen molecule and 3 water molecules depending on different charge state (+1, 0, or -1). Interestingly, in the case of +1 charge, the PbI₆⁻ octahedron at the surface is easily destroyed by interactions with oxygen molecules, while other charge states present stable octahedral structure of PbI₆⁻ with the same surrounding molecules (See **Fig. 4a**). Destroy of PbI₆ octahedral structure in +1 charge state is likely to be mainly attributed to the strong Pb-O bond, which was not shown in neutral and -1 charge state. Furthermore, after Pb-O bond generation, a domino effect of proton transfer from surrounding water molecules finally results in deprotonation of MA⁺ cation which turns into methylamine gases (750 fs of **Fig. 4a**). Such molecular dynamics in +1 charge state will be the reason why the fastest degradation of the ETL/MAPbI₃ device (MAPbI₃ with localized hole) happened in humidified air. In the neutral charge state, oxygen molecules gradually drift apart from the MAPbI₃ surface and water molecules do not react with any MAPbI₃ components (see **Fig. 4b**). Also, the -1 charge state leads to unexpected molecular interactions in that an oxygen molecule attach to iodide anion, but there is no further destroy of PbI₆⁻ octahedron (**Fig. 4c**), which indicates that oxygen cannot directly attack Pb atom at the center of PbI₆ octahedron in the MAPbI₃ crystals with localized electron. To clearly compare intermolecular interactions in these systems, we analyzed Pb-O, I-O and O-H distances for atoms of interest during the simulation, respectively. (**Fig. 4d-f**). In the +1 charge state, Pb and I atoms of MAPbI₃ crystal have the strongest interactions with oxygen molecules, which is evidenced by the shortest Pb-O and I-O distance in **Fig. 4d, e**. On the other hand, there seems to be weak intermolecular interaction between MAPbI₃ components and gaseous molecules in both cases of neutral and -1 charge state (**Fig. 4d-f**). Also, we compared O-H distance to verify the deprotonation of MA⁺ cation. The hydrogen and oxygen atoms are the component of MA⁺

cation and water molecules, respectively. The shortened O-H distance of 1 Å directly indicates the deprotonation of MA⁺ cation, only shown in +1 charge state, not in the other states (See **Fig. 4f**). Overall, intermolecular interactions between MAPbI₃ components and gaseous molecules actively take place when MAPbI₃ crystals are with localized hole, from which the fastest degradation of MAPbI₃ with localized hole can be clearly explained.

Possible scenario on decrystallization of MAPbI₃ crystals under the mixture of O₂ and H₂O

We suggest detailed scenario for degradation mechanisms of MAPbI₃ crystals under the mixture of O₂ and H₂O from experiments and simulation results. In the present AIMD simulation, the mixture makes totally different intermolecular interactions from the situation when O₂ or H₂O solely exist.²⁰ At the beginning state, O₂ molecule is easily adsorbed near the I⁻ anion at the surface of MAPbI₃ regardless of charge state (see filled square line 0-80 fs of **Fig. 4e**), and it attempts to directly interact with Pb atoms (see 0-180 fs of **Fig. 4d**). However, different interplays of H₂O and O₂ molecules with MAPbI₃ components occur depending on charge state (see **Fig. 4e-f**). For the case of +1 charge state (one localized hole), I-O interaction stabilizes (blue filled square line in **Fig. 4e**) and H₂O molecule approaches closely to I-O (blue filled square line in **Fig. 4f**). Since positive charge of Pb atom is partially increased by a localized hole in the MAPbI₃ slab, Pb-O bond is finally formed after 500 fs (see **Fig. 4d**). Then, H₂O molecule could completely provide a proton to Pb-bonded O atom, followed by forming stable hydroxide species (Pb-I-O-OH) (see blue filled square line in **Fig. 4f**). At the same time, MA cation is totally deprotonated by donating proton to deprotonated H₂O (OH⁻) (**Fig. 4f**). Consequently, such generation of hydroxide species and deprotonation of MA cation lead to fast destroy of a MAPbI₃ unit cell.

For the case of -1 charge state (one localized electron), I-O interaction abruptly weakens after 100 fs in **Fig. 4e**, which is likely to be influenced by augmented negative charge of I atom. Sequentially, Pb-O interaction is not strengthened enough to form stable Pb-O bond (see red line of **Fig. 4d**), and then H₂O molecule separates from adsorbed O₂ molecule, which is indicative of no proton transfer (see red square line around 500 – 600 fs of **Fig. 4f**). In this case, PbI₆⁻ octahedron is rather stabilized due to the absence of proton transfer. For the case of neutral charge state (no localized charge), no intermolecular interaction between gas molecules and components of MAPbI₃ occur, which means no degradation of MAPbI₃ crystal (see **Fig. 4b** and black lines of **Fig. 4d-f**). In summary, the decomposition of MAPbI₃ crystals under the mixed ambient of O₂ and H₂O occurs vigorously through deprotonation with localized holes.

X-ray assisted spectroscopic results supporting degradation scenario

To find out experimental evidence of our degradation scenario, we measured and analyzed X-ray assisted spectroscopy data of fresh and degraded MAPbI₃ samples. First, we detected solid Pb(OH)I as one of lead hydroxide products appearing at the peak of 38.7° from X-ray diffraction patterns (XRD) of degraded MAPbI₃ films in **Fig. 5a**.³⁵ These results agree with the generation of lead hydroxide species in our AIMD simulation in the mixed ambient of O₂ and H₂O. Additionally, the existence of hydroxide was also observed from comparison of X-ray photoelectron spectroscopy (XPS) data for the fresh and degraded MAPbI₃ film. As shown in **Fig. 5b**, O1s peak shifts to higher binding energy region for the degraded sample, which means that O-H bonding character is reinforced.³⁶⁻³⁸ In other words, it is certain that hydroxide species are produced as an end product of degradation as we supposed above. XPS spectra bring out another crucial evidence in terms of iodine loss. **Fig. 5c** shows XPS spectra of fresh MAPbI₃, the degraded ETL/MAPbI₃, and the degraded HTL/MAPbI₃ within the range

from 135 eV to 140 eV. In the fresh sample, only Pb-I bond is detected as known from Pb 4f_{7/2} peak appearing at 138.0 eV. After the degradation, the distinct peak of 136.3 eV corresponding to metallic Pb appear in both cases of the ETL/MAPbI₃ and HTL/MAPbI₃ sample, which is indicative of iodine loss, namely the complete destruction of PbI₆⁻ octahedral.³⁹⁻⁴¹ The peak intensity of the ETL/MAPbI₃ is much higher than that of the HTL/MAPbI₃, which is consistent with our simulation results in that MAPbI₃ crystal is more stable at the +1 charge state, as compared to the -1 charge state.

Conclusions

We observed different light-induced degradation rates of MAPbI₃ films depending on the charge polarity selectivity of underlying transporting layer under various surrounding ambient conditions. It was confirmed that localized carrier polarity inside of MAPbI₃ film incurred by charge selectivity of the underlying layer plays a decisive role in determining the degradation rate of MAPbI₃ films. The MAPbI₃ films with localized hole degraded more rapidly in the presence of H₂O than ones with localized electron, whereas inverted trend of degradation rate appeared under O₂-only ambient. Interestingly, the combination of H₂O and O₂ led to the fastest degradation of the MAPbI₃ film only with localized hole, where the MAPbI₃ film with localized electron unexpectedly stabilized in contrast to the case of O₂-only condition. To explain these observations, we investigated intermolecular dynamics of H₂O, O₂ and components of MAPbI₃ through DFT-based AIMD simulations. The dramatic difference in degradation rates under mixed atmosphere condition is mainly attributed to the generation of strong Pb-O interaction and lead hydroxide species at the hole localized MAPbI₃ crystal, which was evidenced by XPS and XRD results. Our study suggests that the positive localized charge in the MAPbI₃ crystals drives fast de-crystallization under actual atmospheric conditions, which provide the direction for long-term stability of perovskite solar cells.

Methods

Materials and device fabrication

All materials were used as received. The ITO glass substrates (AMG, $9.5 \Omega \text{ cm}^{-2}$) were cleaned by sonication in acetone, isopropanol, and deionized water followed by the deposition of the transporting materials. A 35 nm thick C_{60} layer was coated onto the ITO glass substrate using a vacuum thermal evaporator at a deposition rate of $0.2 \text{ \AA} \cdot \text{s}^{-1}$ and pressure of 10^{-7} Torr. A single PCBM layer was spin-coated at a rotation speed of 2,000 rpm. for 60 s using its 10 mg/mL solution in chlorobenzene (Sigma-Aldrich) and then annealed at a temperature of 100 °C for 10 min. A Spiro-MeOTAD (Merk) layer was drop-cast on a spinning substrate at rotation speed of 3,000 rpm for 30 s using its 72.3 mg/mL solution in chlorobenzene. A PEDOT: PSS (Clevios, AI4083) layer was spin-coated at a speed of 5,000 rpm for 40 s using its 1:1 (v/v) diluted solution in deionized water and then annealed at 130 °C for a minimum of 30 min. MAPbI_3 perovskite solutions were prepared by mixing PbI_2 (Alfa Aesar), MAI (Xian' Chemical), dimethyl sulfoxide (DMSO, Sigma-Aldrich), and dimethylformamide (DMF, Sigma-Aldrich) at specified proportions. For example, to prepare 52 wt.% of precursor in DMF solvent with the molecular ratio $\text{PbI}_2:\text{MAI}:\text{DMSO} = 1:1:1$, 461 mg of PbI_2 , 159 mg of MAI, and 78 mg of dimethyl sulfoxide were mixed in 0.60 mL of DMF. After spin coating the obtained precursor at a speed of 4,000 rpm for 20 s combined with a diethyl ether dripping procedure, the resulting intermediate films were annealed at 100 °C for 10 min. All spin coating procedures in this study were performed inside a dry room with a relative humidity of less than 10% and temperature of 25 °C.

Ageing conditions

All perovskite films were exposed to light in a controlled environment by customized

chamber. Dry air condition was configured by supplying dry air gas (80 % nitrogen / 20 % oxygen) as 0.5 liter/m. H₂O condition was configured by supplying nitrogen gas with H₂O bubbler as 0.5 liter/m. The mixed ambient condition was configured by supplying dry air gas with H₂O bubbler as 0.5 liter/m. Light illumination was performed under 1 sun condition using an AAA solar simulator (Newport Oriel Solar 3A Class AAA, 64023A). The light intensity was calibrated using a KG-5 standard silicon solar cell (Oriel, VLSI Standards).

Characterization

Time-resolved and steady-state PL measurements were conducted using a FluoroMax-4 spectrofluorometer (Horiba). The studied films were photo-excited with a 463-nm laser diode (DeltaDiode-470L, Horiba) pulsed at a frequency of 100 MHz. The resulting PL was detected by a high-sensitivity photon counting near infrared (NIR) detector. Planar SEM and cross-sectional images of the perovskite solar cell structure were obtained using a field-emission scanning electron microscope (FESEM, AURIGA, Carl Zeiss) combined with a focused ion beam system (FIB system, AURIGA, Carl Zeiss). The absorbance spectra and crystalline diffraction patterns were recorded using an ultraviolet-visible/NIR spectrophotometer (Cary 5000, Agilent Technologies) and an X-ray diffractometer (New D8 Advanced, Bruker), respectively. The XPS spectra were obtained using an electron spectroscopy for chemical analysis instrument (Sigma Probe, VG Systems). SKPM measurements was performed in a non-contact mode using an atomic force microscope (NX10, Park Systems) equipped with an NSC36/Cr-Au tip.

DFT calculation

The DFT calculations were conducted using the projector augmented wave (PAW) method and generalized gradient approximation of Perdew, Burke, and Ernzerhof (PBE) for the exchange-

correlation potential implemented in the Vienna Ab-initio Simulation Package (VASP) code. The lattice parameters a and c of the tetragonal $(\text{CH}_3\text{NH}_3)\text{PbI}_3$ lattice were 8.86 Å and 12.66 Å for 4 unit cells, respectively. Monkhorst-Pack k-point sampling with $4\times 4\times 2$ k-point grids was used for the Brillouin zone integration. An energy cutoff of 500 eV was used to expand the wavefunctions in the plane-wave representation. Atomic structures were relaxed until all Hellman-Feynman forces were below 0.01 eV/Å. A climbing-image nudged elastic band method was used for locating minimum energy pathways.

Acknowledgements

This work has been supported by the Global Frontier R&D Program of the Center for Multiscale Energy Systems funded by the National Research Foundation under the Ministry of Science and ICT, Korea (2012M3A6A7054855). This work has been also supported by the National Research Foundation under the Ministry of Science and ICT, Korea. (2017R1A2B3010927). The XRD patterns were measured at Research Institute of Advanced Materials in Seoul National University.

Author contributions

M.-c.K., N.A., Y.U.J., H.S.J. and M.C. conceived and designed the experiments. M.-c.K. performed the half device fabrication and carried out the controlled stability test. M.-c.K. and N. A. measured KPFM. M.-c.K., N.A., and P.V.P discussed the mechanism of charge unbalance generation in MAPbI₃. E.L and S.K.K calculated the DFT simulations. M.-c.K., N.A., H.S.J. and M.C. wrote the paper. All authors discussed the results.

References

1. N. Ahn, D.-Y. Son, I.-H. Jang, S. M. Kang, M. Choi and N.-G. Park, *Journal of the American Chemical Society*, 2015, **137**, 8696-8699.
2. H. S. Kim, C. R. Lee, J. H. Im, K. B. Lee, T. Moehl, A. Marchioro, S. J. Moon, R. Humphry-Baker, J. H. Yum, J. E. Moser, M. Gratzel and N. G. Park, *Scientific reports*, 2012, **2**, 591.
3. A. Kojima, K. Teshima, Y. Shirai and T. Miyasaka, *Journal of the American Chemical Society*, 2009, **131**, 6050-6051.
4. W. S. Yang, B.-W. Park, E. H. Jung, N. J. Jeon, Y. C. Kim, D. U. Lee, S. S. Shin, J. Seo, E. K. Kim and J. H. Noh, *Science*, 2017, **356**, 1376-1379.
5. D. Bryant, N. Aristidou, S. Pont, I. Sanchez-Molina, T. Chotchunangatchaval, S. Wheeler, J. R. Durrant and S. A. Haque, *Energy & Environmental Science*, 2016, **9**, 1655-1660.
6. J. A. Christians, P. A. Miranda Herrera and P. V. Kamat, *Journal of the American Chemical Society*, 2015, **137**, 1530-1538.
7. J.-H. Lee, N. C. Bristowe, P. D. Bristowe and A. K. Cheetham, *Chemical Communications*, 2015, **51**, 6434-6437.
8. I. A. Shkrob and T. W. Marin, *The journal of physical chemistry letters*, 2014, **5**, 1066-1071.
9. Z. Zhu, V. G. Hadjiev, Y. Rong, R. Guo, B. Cao, Z. Tang, F. Qin, Y. Li, Y. Wang and F. Hao, *Chemistry of Materials*, 2016, **28**, 7385-7393.
10. G. Niu, X. Guo and L. Wang, *Journal of Materials Chemistry A*, 2015, **3**, 8970-8980.
11. N. Aristidou, I. Sanchez- Molina, T. Chotchuangchutchaval, M. Brown, L. Martinez, T. Rath and S. A. Haque, *Angewandte Chemie International Edition*, 2015, **54**, 8208-8212.
12. G. Divitini, S. Cacovich, F. Matteocci, L. Cina, A. Di Carlo and C. Ducati, *Nature Energy*, 2016, **1**, 15012.
13. A. Guerrero, J. You, C. Aranda, Y. S. Kang, G. Garcia-Belmonte, H. Zhou, J. Bisquert and Y. Yang, *Acs Nano*, 2015, **10**, 218-224.
14. Y. Han, S. Meyer, Y. Dkhissi, K. Weber, J. M. Pringle, U. Bach, L. Spiccia and Y.-B. Cheng,

- Journal of Materials Chemistry A*, 2015, **3**, 8139-8147.
15. T. A. Berhe, W.-N. Su, C.-H. Chen, C.-J. Pan, J.-H. Cheng, H.-M. Chen, M.-C. Tsai, L.-Y. Chen, A. A. Dubale and B.-J. Hwang, *Energy & Environmental Science*, 2016, **9**, 323-356.
 16. S. Yang, W. Fu, Z. Zhang, H. Chen and C.-Z. Li, *Journal of Materials Chemistry A*, 2017, **5**, 11462-11482.
 17. T. Leijtens, E. T. Hoke, G. Grancini, D. J. Slotcavage, G. E. Eperon, J. M. Ball, M. De Bastiani, A. R. Bowring, N. Martino, K. Wojciechowski, M. D. McGehee, H. J. Snaith and A. Petrozza, *Advanced Energy Materials*, 2015, **5**, 1500962.
 18. S. Bae, S. Kim, S.-W. Lee, K. J. Cho, S. Park, S. Lee, Y. Kang, H.-S. Lee and D. Kim, *The journal of physical chemistry letters*, 2016, **7**, 3091-3096.
 19. N. Ahn, K. Kwak, M. S. Jang, H. Yoon, B. Y. Lee, J.-K. Lee, P. V. Pikhitsa, J. Byun and M. Choi, *Nature communications*, 2016, **7**, 13422.
 20. K. Kwak, E. Lim, N. Ahn, J. Heo, K. Bang, S. K. Kim and M. Choi, *arXiv preprint arXiv:1709.04130*, 2017.
 21. M.-c. Kim, MRS 2017 Fall Meeting ES01.07.15, Boston, USA, 2017.
 22. M.-c. Kim, Ph. D Engineering Doctorate, Seoul National University, 2018.
 23. E. M. Hutter, J.-J. Hofman, M. L. Petrus, M. Moes, R. D. Abellón, P. Docampo and T. J. Savenije, *Advanced Energy Materials*, 2017, **7**, 1602349.
 24. K. Wojciechowski, T. Leijtens, S. Siprova, C. Schlueter, M. T. Hörantner, J. T.-W. Wang, C.-Z. Li, A. K.-Y. Jen, T.-L. Lee and H. J. Snaith, *The journal of physical chemistry letters*, 2015, **6**, 2399-2405.
 25. J. Seo, S. Park, Y. C. Kim, N. J. Jeon, J. H. Noh, S. C. Yoon and S. I. Seok, *Energy & Environmental Science*, 2014, **7**, 2642-2646.
 26. J. H. Heo, H. J. Han, D. Kim, T. K. Ahn and S. H. Im, *Energy & Environmental Science*, 2015, **8**, 1602-1608.
 27. M. Saliba, T. Matsui, J.-Y. Seo, K. Domanski, J.-P. Correa-Baena, M. K. Nazeeruddin, S. M. Zakeeruddin, W. Tress, A. Abate and A. Hagfeldt, *Energy & Environmental Science*, 2016, **9**,

1989-1997.

28. S. D. Stranks, V. M. Burlakov, T. Leijtens, J. M. Ball, A. Goriely and H. J. Snaith, *Physical Review Applied*, 2014, **2**, 034007.
29. H. Greijer, J. Lindgren and A. Hagfeldt, *The Journal of Physical Chemistry B*, 2001, **105**, 6314-6320.
30. J. Liu, Y. Wu, C. Qin, X. Yang, T. Yasuda, A. Islam, K. Zhang, W. Peng, W. Chen and L. Han, *Energy & Environmental Science*, 2014, **7**, 2963-2967.
31. P. Zhao, W. Yin, M. Kim, M. Han, Y. J. Song, T. K. Ahn and H. S. Jung, *Journal of Materials Chemistry A*, 2017, **5**, 7905-7911.
32. C. Motta, F. El-Mellouhi and S. Sanvito, *Scientific reports*, 2015, **5**, 12746.
33. F. Mohn, L. Gross, N. Moll and G. Meyer, *Nature nanotechnology*, 2012, **7**, 227-231.
34. W. Nie, J.-C. Blancon, A. J. Neukirch, K. Appavoo, H. Tsai, M. Chhowalla, M. A. Alam, M. Y. Sfeir, C. Katan and J. Even, *Nature communications*, 2016, **7**, 11574.
35. A. Babayigit, D. D. Thanh, A. Ethirajan, J. Manca, M. Muller, H.-G. Boyen and B. Conings, *Scientific reports*, 2016, **6**, 18721.
36. K.-H. Jung, J.-Y. Seo, S. Lee, H. Shin and N.-G. Park, *Journal of Materials Chemistry A*, 2017, **5**, 24790-24803.
37. H. L. Mosbacker, Y. M. Strzhemechny, B. D. White, P. E. Smith, D. C. Look, D. C. Reynolds, C. W. Litton and L. J. Brillson, *Applied Physics Letters*, 2005, **87**, 012102.
38. M. M. Sabri, J. Jung, D. H. Yoon, S. Yoon, Y. J. Tak and H. J. Kim, *Journal of Materials Chemistry C*, 2015, **3**, 7499-7505.
39. B. Conings, J. Drikkoningen, N. Gauquelin, A. Babayigit, J. D'Haen, L. D'Olieslaeger, A. Ethirajan, J. Verbeeck, J. Manca and E. Mosconi, *Advanced Energy Materials*, 2015, **5**.
40. G. R. Kumar, A. D. Savariraj, S. Karthick, S. Selvam, B. Balamuralitharan, H.-J. Kim, K. K. Viswanathan, M. Vijaykumar and K. Prabakar, *Physical Chemistry Chemical Physics*, 2016, **18**, 7284-7292.
41. T.-W. Ng, C.-Y. Chan, M.-F. Lo, Z. Q. Guan and C.-S. Lee, *Journal of Materials Chemistry A*,

2015, **3**, 9081-9085.

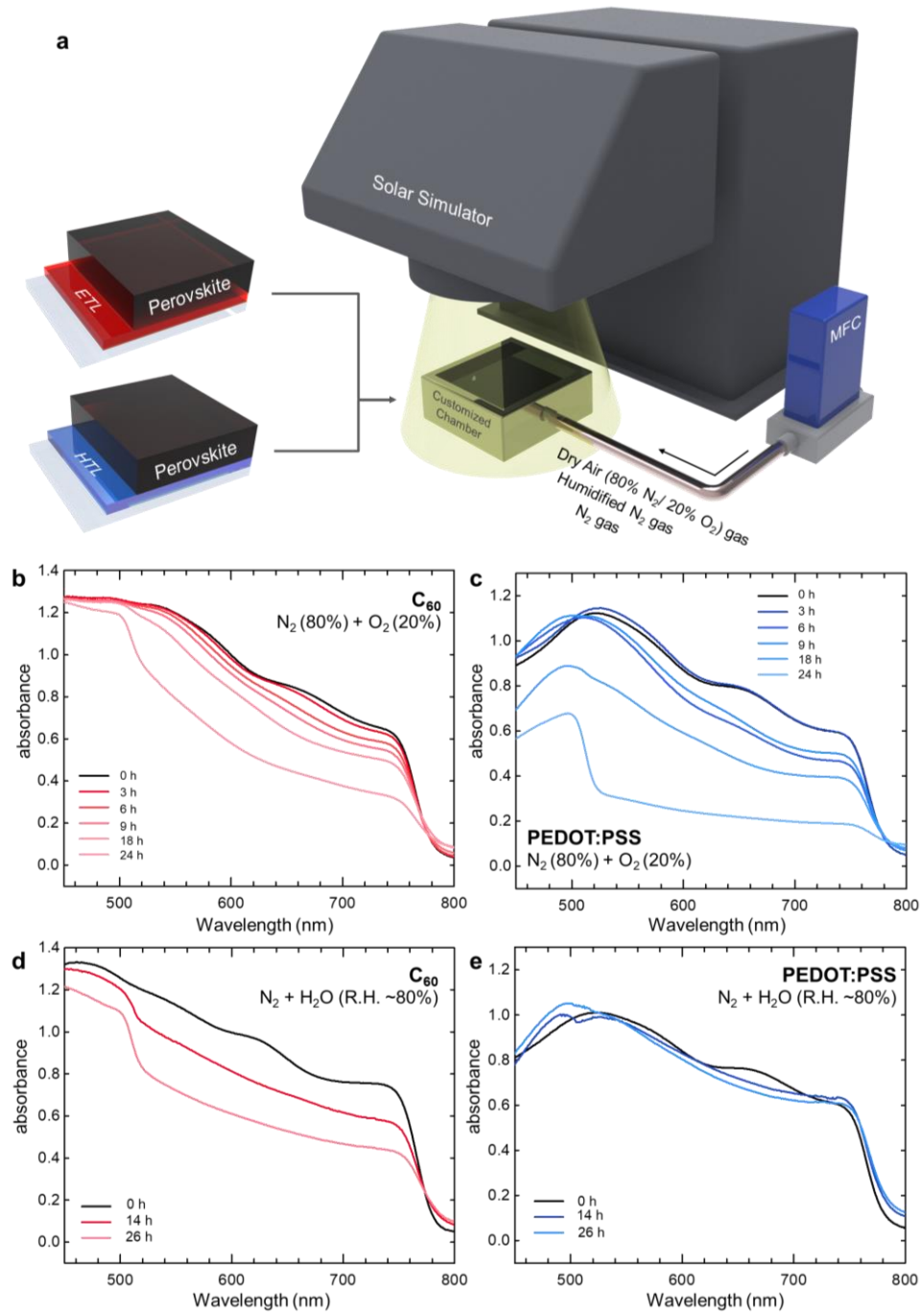


Fig. 1. Light-induced degradation test of perovskite films depending on the excessive charge polarity under different atmospheric conditions. (a) Schematics of customized experimental systems for light-induced degradation with solar simulator, customized chamber and gas flow controller. Time evolution of absorption spectra for (b) the C₆₀/MAPbI₃ (hole-rich) and (c) the PEDOT:PSS/MAPbI₃ (electron-rich) half devices in a chamber filled with dry air (80% nitrogen and 20% oxygen). Time evolution of absorption spectra for (d) the C₆₀/MAPbI₃ and (e) the PEDOT:PSS/MAPbI₃ half devices in a chamber filled with nitrogen and water vapors (R.H. ~80%). Every samples were under continuous light illumination except when measuring absorption spectra.

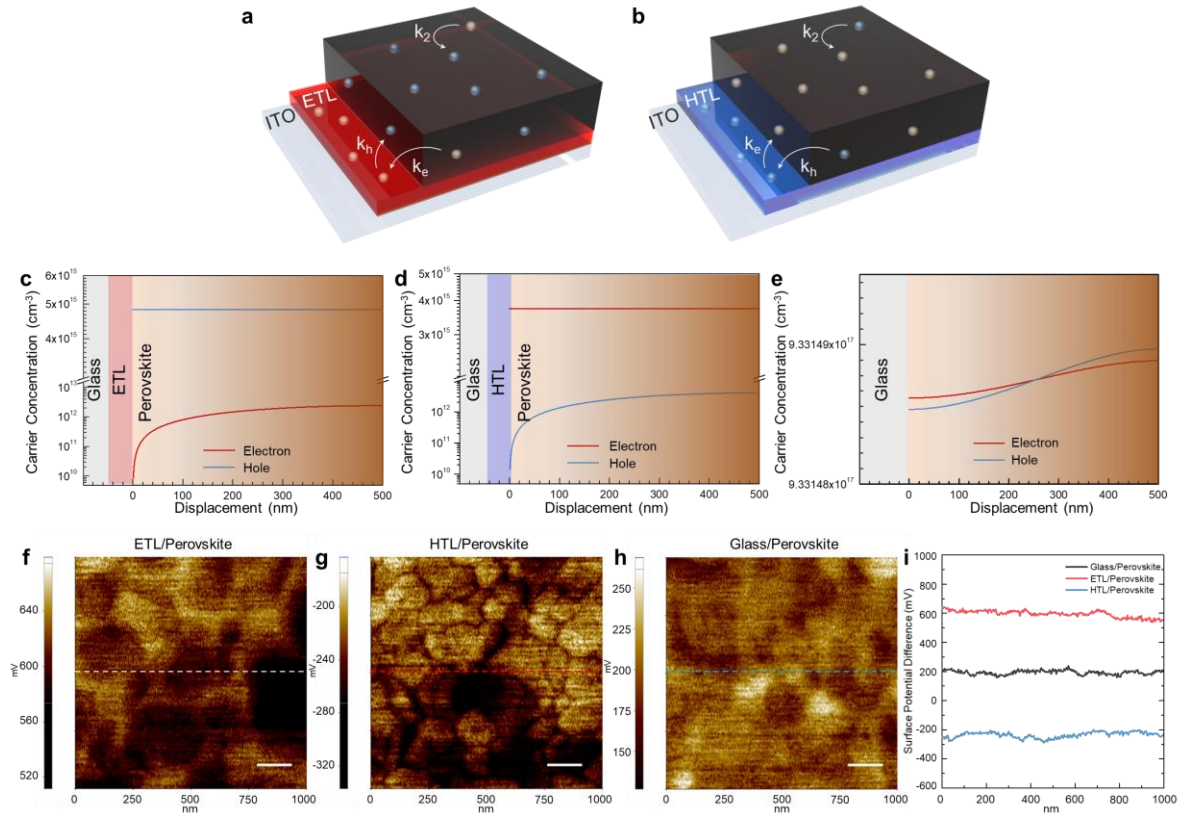


Fig. 2. Unbalance of charge polarity for charge-selective transporting half devices. Schematics of the experimental setup and charge-selective transporting half devices ((a)ETL/MAPbI₃ and (b)HTL/MAPbI₃ ones). Calculated carrier concentration as a function of thickness displacement for MAPbI₃ film deposited on (c) Glass/ETL, (d) Glass/HTL and (e) Glass substrate. Surface potential energy distribution images measured by scanning Kelvin probe microscopy (SKPM) for MAPbI₃ film deposited on (f) C₆₀ (ETL), (g) PEDOT:PSS (HTL) and (h) glass substrate. (i) Surface potential plot along the marked line in (f-h) respectively. All the scale bars are 150 nm.

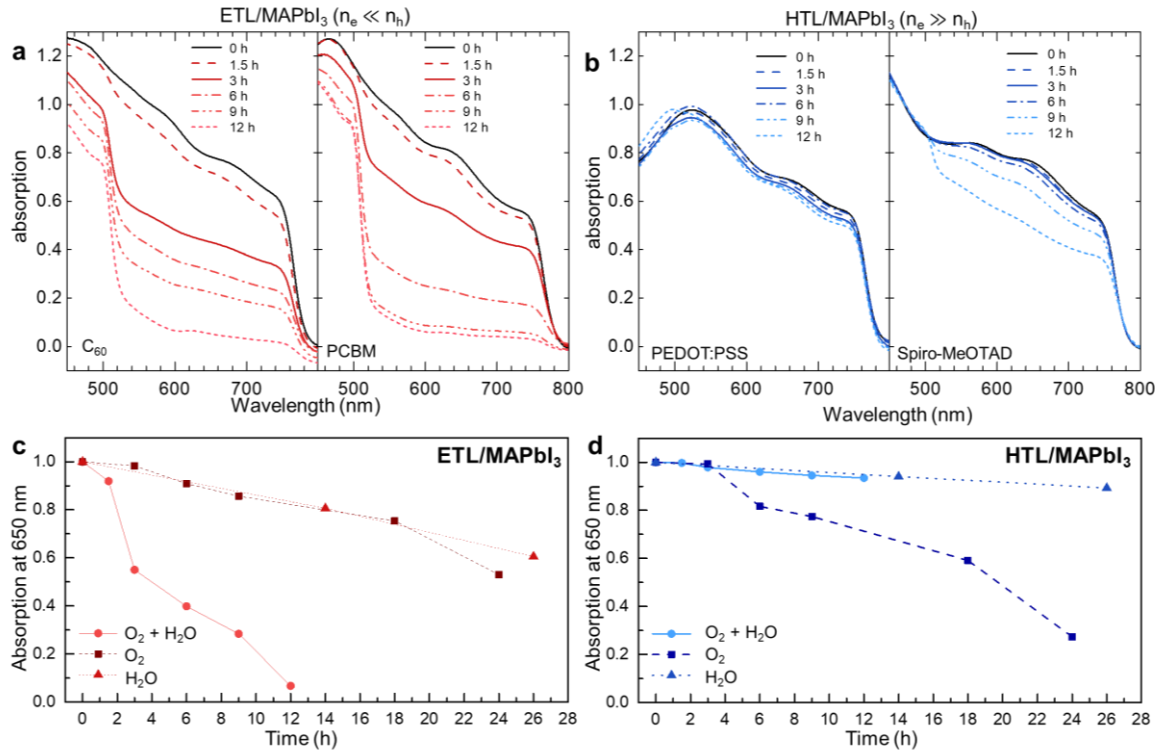


Fig. 3. Light-induced degradation under the mixture ambient of O₂ and H₂O depending on localized charge polarity. Time evolution of absorption spectra from 0 h to 12 h for (a) ETL/MAPbI₃ and (b) HTL/MAPbI₃ samples. C₆₀, PCBM were used for ETL/MAPbI₃ configuration and PEDOT:PSS, Spiro-MeOTAD for HTL/MAPbI₃ configuration. Time evolution of absorption spectra are summarized by plotting absorption peak at 650 nm for (c) ETL/MAPbI₃ and (d) HTL/MAPbI₃ under 3 different ambient conditions (the mixture ambient, O₂ (20%) ambient and H₂O (R.H. ~80%) ambient).

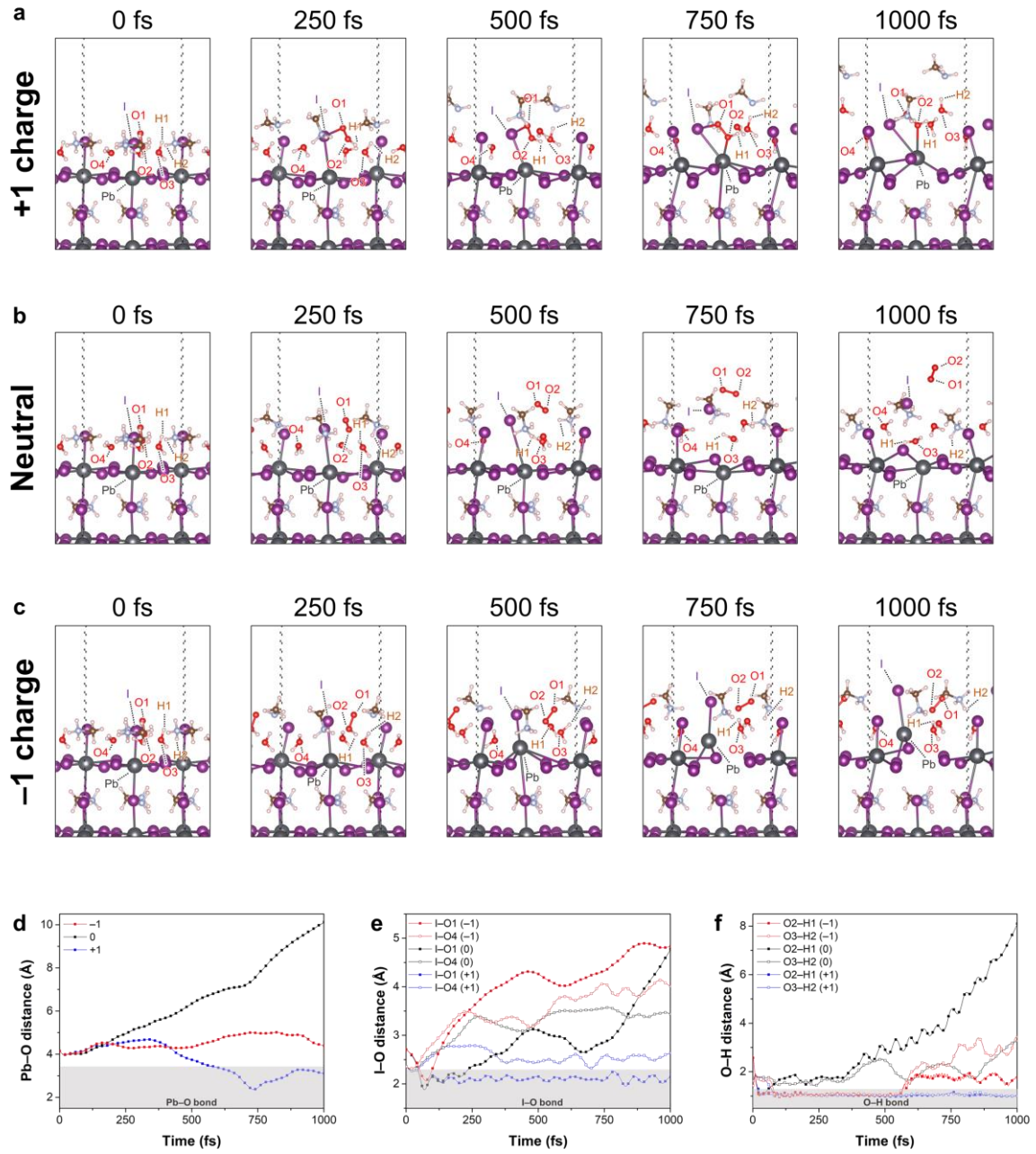


Fig. 4. AIMD simulation results. Time evolution of molecular dynamic simulations of MAPbI₃ surface for (a) +1 unit charge, (b) neutral, (c) -1 unit charge under 3 H₂O and 1 O₂ ambient atmosphere. Atomic bonding distance of (d) Pb-O, (e) I-O, (f) O-H bond respectively.

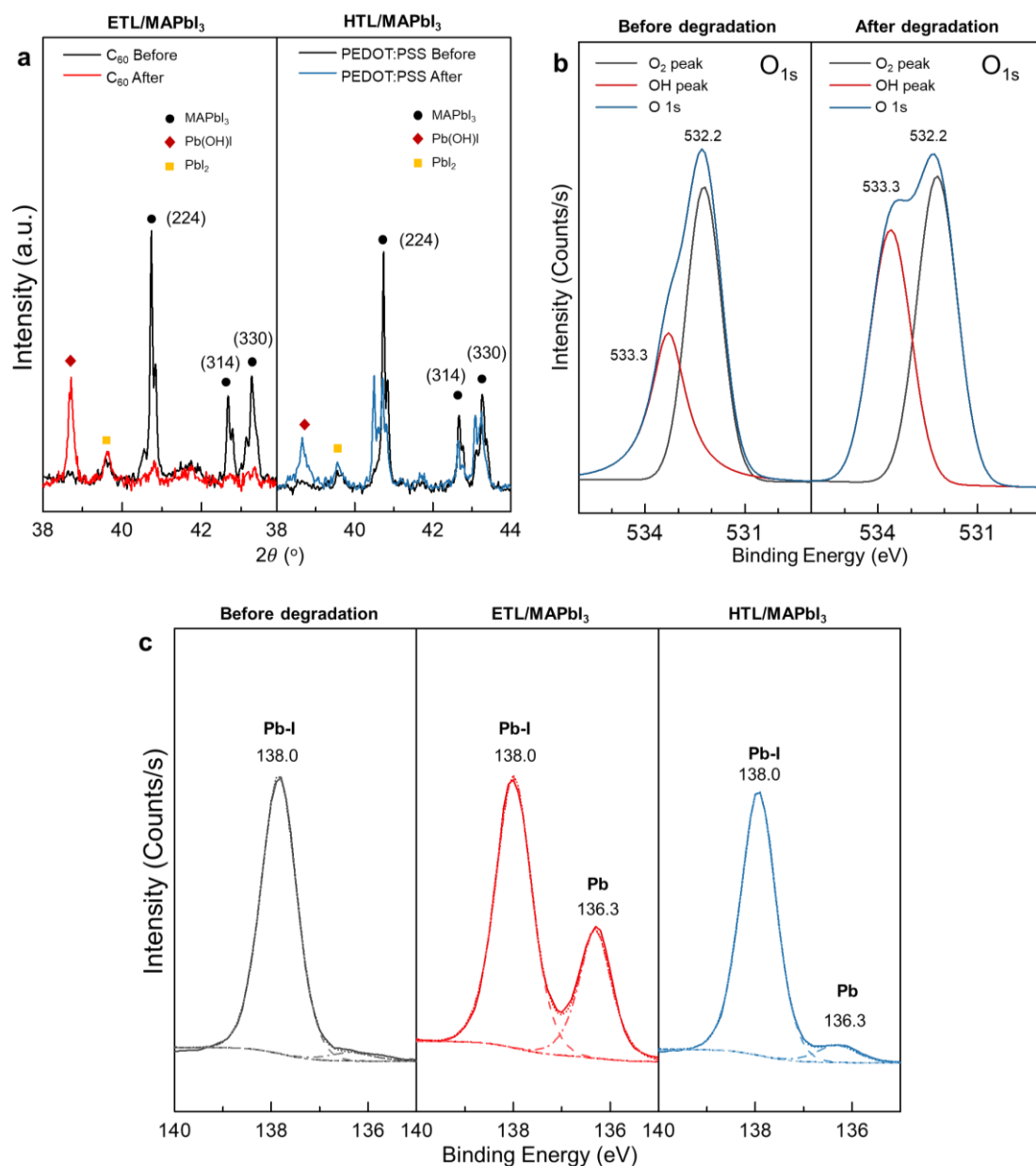


Fig. 5. Observation of hydroxide species and Metallic Pb as the result of light-induced perovskite film degradation. (a) XRD patterns of degraded MAPbI₃ films deposited on ETL and HTL at the range between 38° to 44° 2θ. MAPbI₃, Pb(OH)I and PbI₂ peaks are indexed respectively. (b) XPS spectra recorded for the O atom (O1s) of the ETL/MAPbI₃ film before and after degradation (c) XPS spectra recorded for the Pb atom (Pb 4f_{7/2}) of the fresh, ETL/MAPbI₃ and HTL/MAPbI₃ samples.

Decrystallization of CH₃NH₃PbI₃ perovskite crystals via polarity dependent localized charges

Min-cheol Kim^{a†}, Namyoung Ahn^{a†}, Eunhak Lim^b, Young Un Jin^c, Peter V. Pikhitsa^a, Jiyoung Heo^d, Seong Keun Kim^b, Hyun Suk Jung^{c} and Mansoo Choi^{a,e*}*

^aGlobal Frontier Center for Multiscale Energy Systems, Seoul National University, Seoul, Republic of Korea.

^bDepartment of Chemistry, Seoul National University, Seoul, Republic of Korea.

^cSchool of Advanced Materials Science & Engineering, Sungkyunkwan University, Suwon, Gyeonggi-do, Republic of Korea.

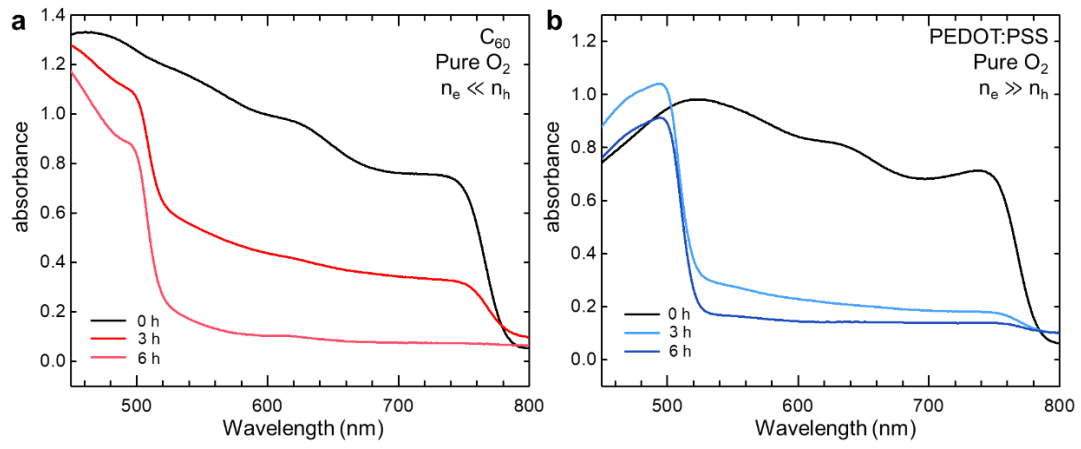
^dDepartment of Green Chemical Engineering, Sangmyung University, Seoul, Republic of Korea.

^eDepartment of Mechanical Engineering, Seoul National University, Seoul, Republic of Korea.

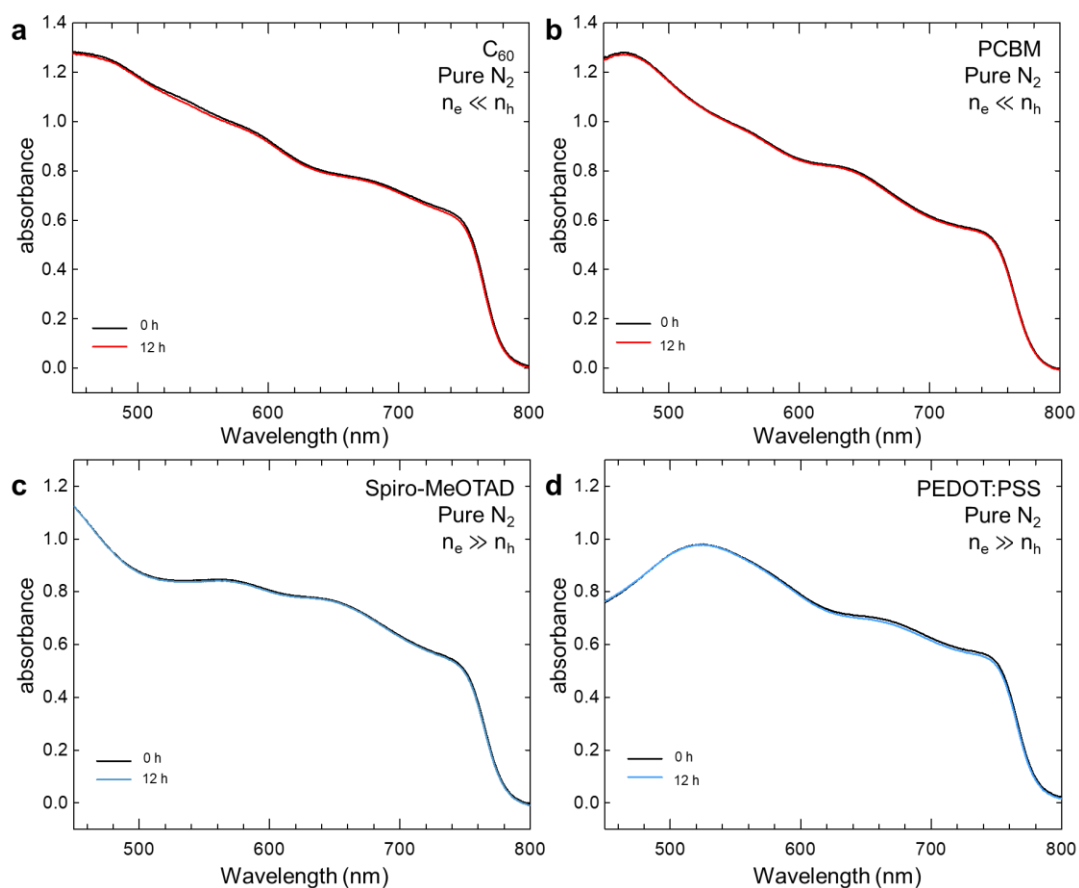
[†]These authors contributed equally to this work.

*Correspondence and request for materials should be addressed to H.S.J. and M. C.

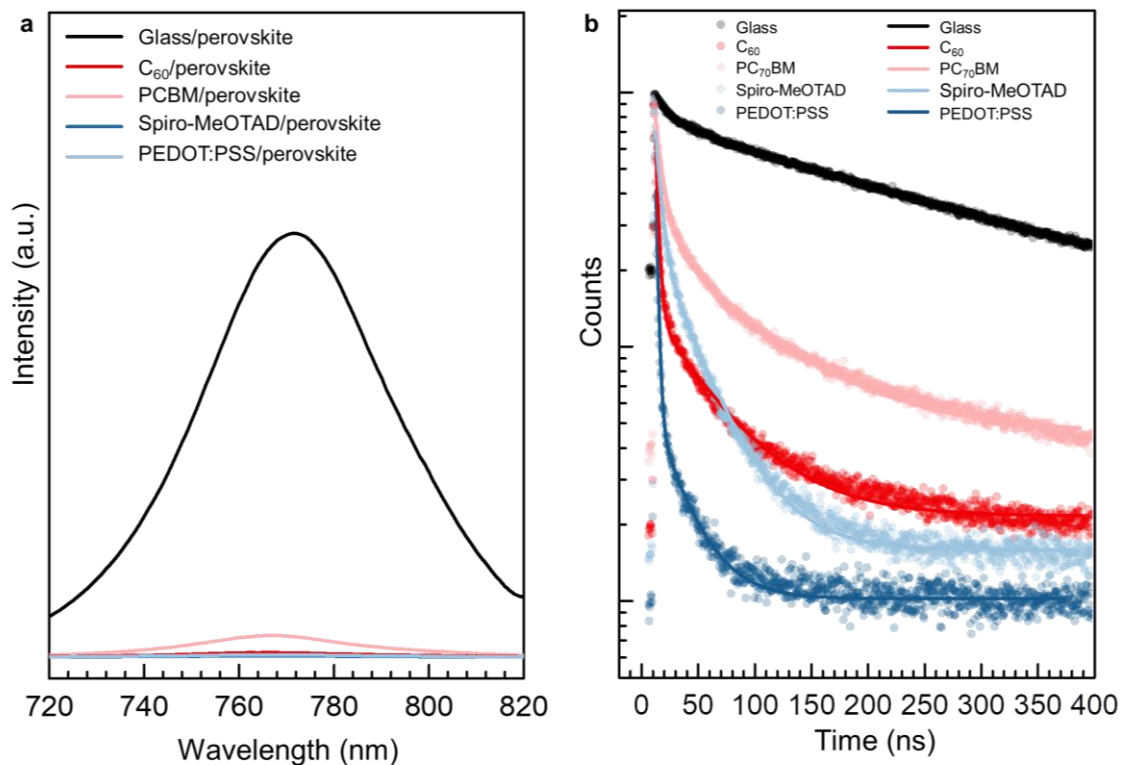
(email: hsjung1@skku.edu; mchoi@snu.ac.kr)



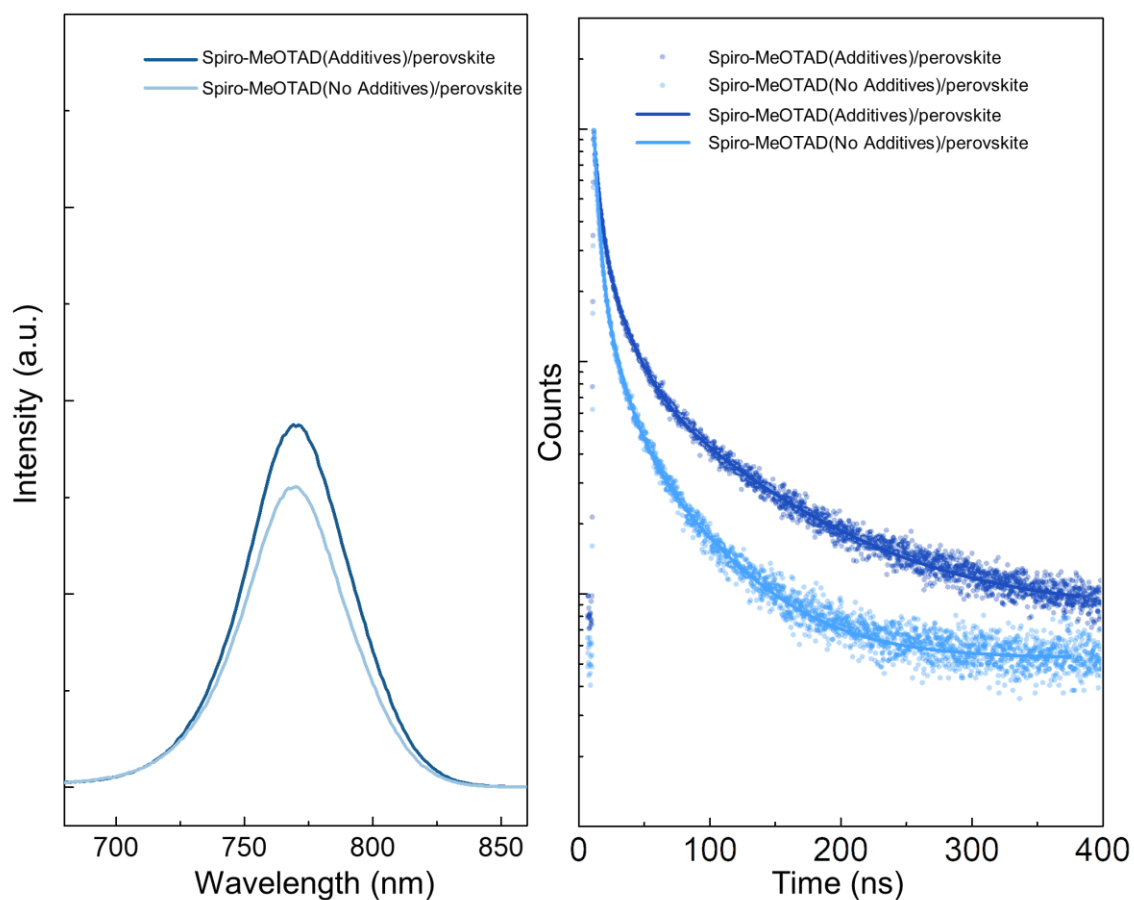
Supplementary Figure 1. Time evolution of absorption spectra for (a) the C₆₀/MAPbI₃ and (b) the PEDOT:PSS/MAPbI₃ half devices in chamber filled with pure O₂ gas before and after light-illumination for 6 h.



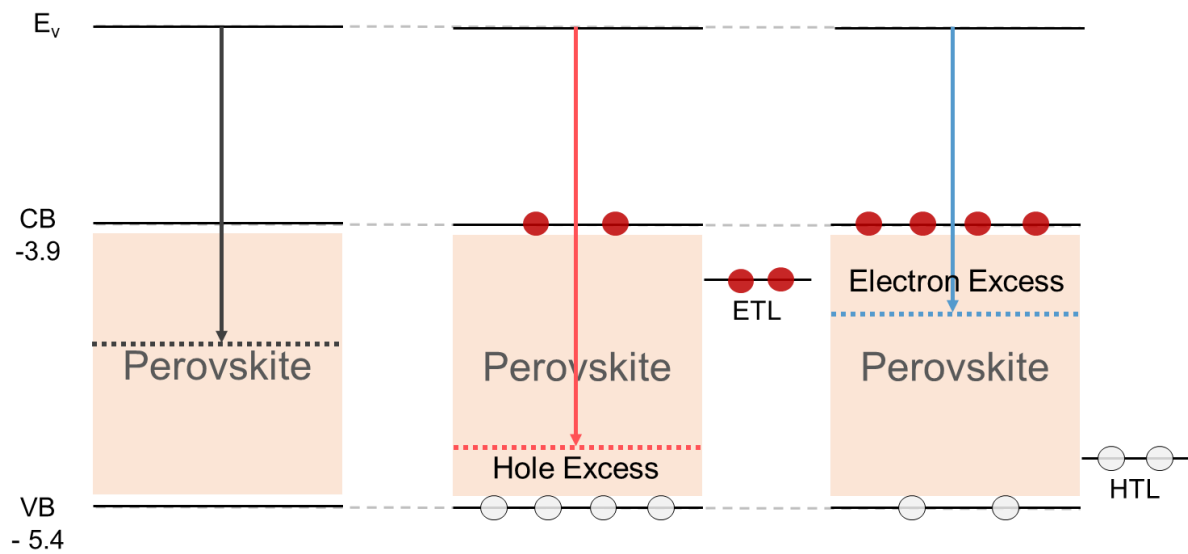
Supplementary Figure 2. Absorption spectra of perovskite films deposited on (a) C_{60} , (b) PCBM, and perovskite films deposited on (c) Spiro-MeOTAD and (d) PEDOT:PSS in chamber filled with pure N_2 gas before and after light-illumination for 12 h.



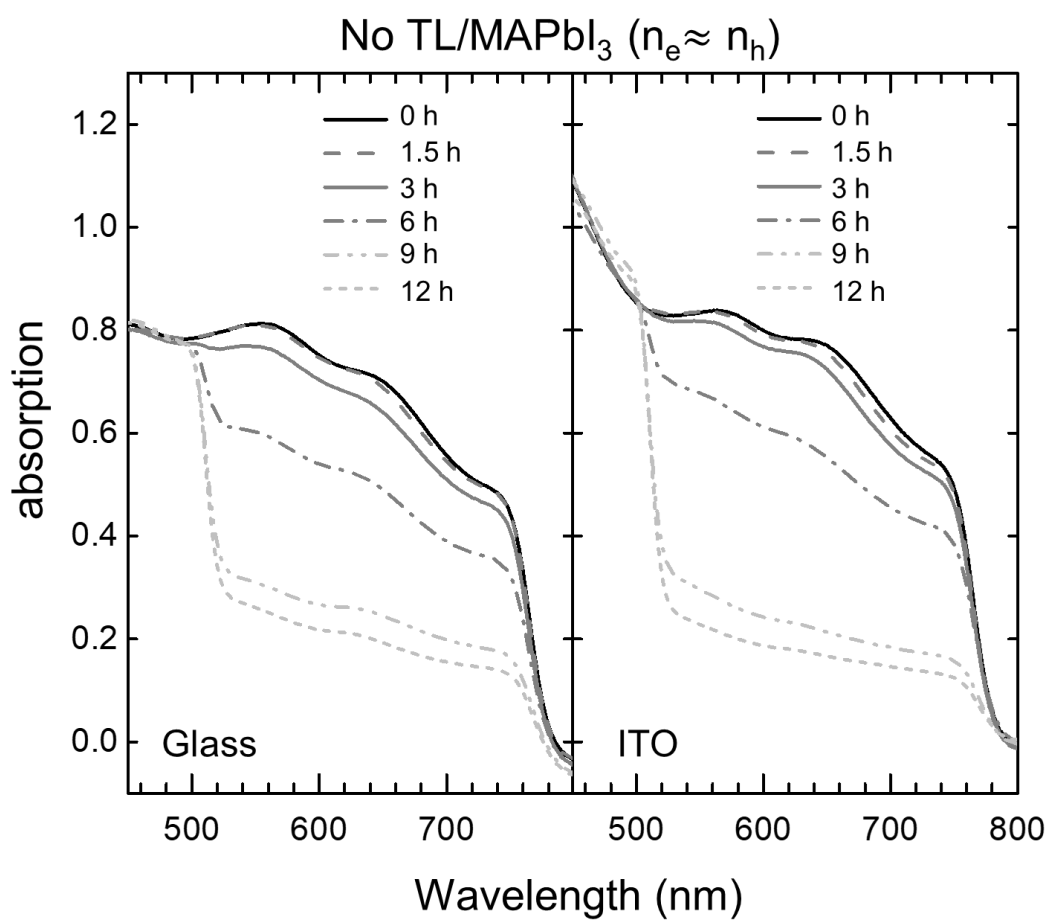
Supplementary Figure 3. (a) Steady-state and (b) time-resolved PL spectra obtained for the perovskite films deposited on the glass, PCBM, C₆₀, Spiro-MeOTAD, and PEDOT:PSS substrates and fitted with the three-term exponential decay function. Time-resolved PL spectra is plotted as circle, and fitted function is plotted as line.



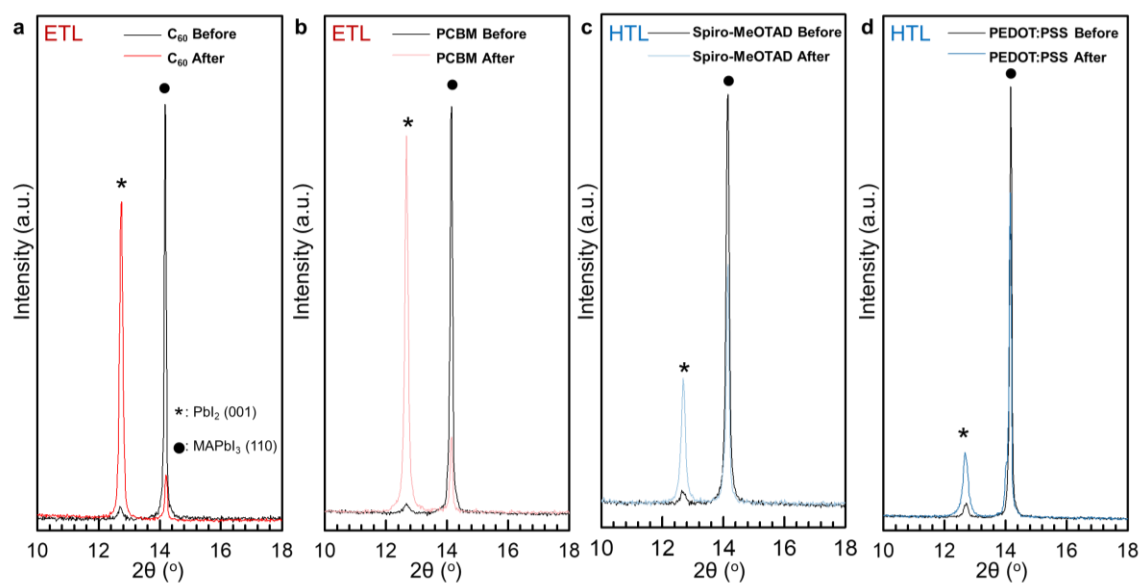
Supplementary Figure 4. (a) Steady-state and (b) time-resolved PL spectra obtained for the perovskite films deposited on the Spiro-MeOTAD with and without additives (such as tBP and Li-TFSI). The data fitted with the three-term exponential decay function.



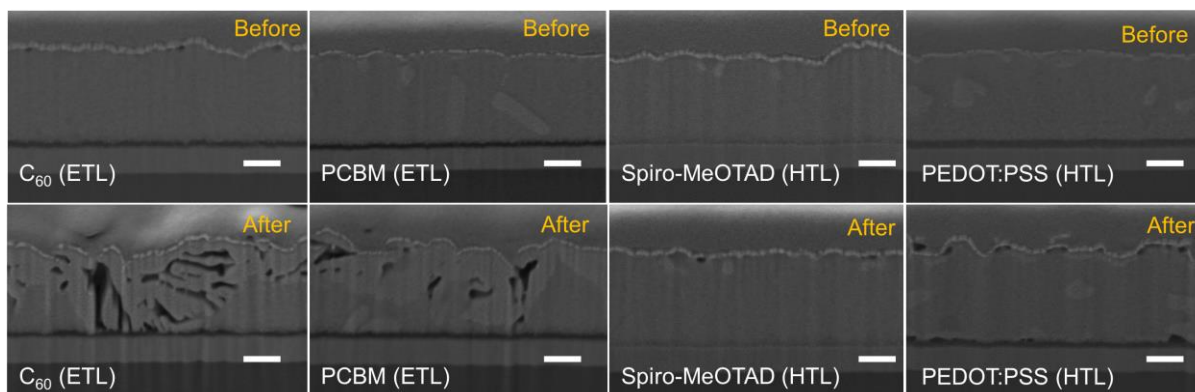
Supplementary Figure 5. Band energy diagram for perovskite films deposited on (a) glass, (b) ETL, and (c) HTL. Quasi fermi level of each films altered due to imbalance of electron-hole carrier concentration. Hole-excess perovskite film deposited on ETL presented lower quasi fermi level, therefore higher surface potential (work function). On the other hands, electron-excess perovskite film on HTL showed lower surface potential.



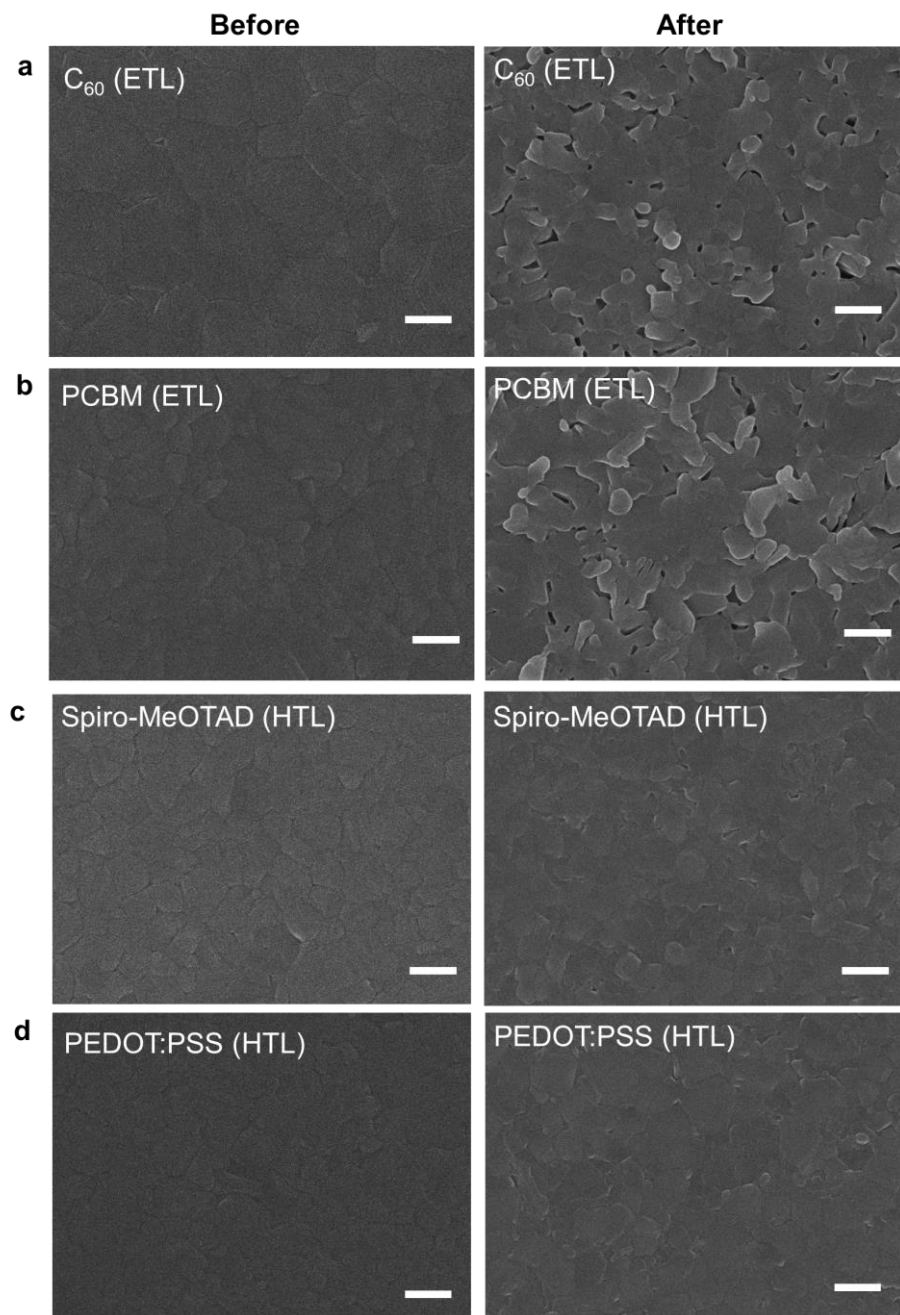
Supplementary Figure 6. (a) Steady-state and (b) time-resolved PL spectra obtained for the perovskite layers deposited on the Spiro-MeOTAD with and without additives (such as tBP and Li-TFSI). The data fitted with the three-term exponential decay function.



Supplementary Figure 7. XRD reflections of the (a) C₆₀, (b) PCBM, (c) Spiro-MeOTAD, and (d) PEDOT:PSS phases in the 2θ range of 10–18°. PbI₂ species are detected at 12.7°, and MAPbI₃ species are detected at 14.2°.



Supplementary Figure 8. The cross-sectional SEM images of the (e) C₆₀, (f) PCBM, (g) Spiro-MeOTAD, and (h) PEDOT:PSS layers obtained by using a focused ion beam before and after light exposure for 3 h. All scale bars are equal to 200 nm.



Supplementary Figure 9. Plane-view SEM images of the perovskite layers deposited on the (a) C₆₀, (b) PCBM, (c) Spiro-MeOTAD, and (d) PEDOT:PSS substrates before and after 6 h of light-soaking. All scale bars are equal to 300 nm.

	A₁(%)	τ₁ (ns)	A₂(%)	τ₂ (ns)	A₃(%)	τ₃ (ns)	Avg. τ
Glass	0.36	7.87	1.64	31.95	98.00	332.89	332.38
C₆₀	13.93	1.99	26.65	22.02	59.42	103.82	96.33
PCBM	6.80	3.86	24.24	28.96	68.96	151.07	143.03
PEDOT:PSS	12.11	3.76	48.01	20.99	48.01	52.69	43.15
Spiro-MeOTAD	25.88	1.47	20.82	5.17	53.30	32.97	30.77

Supplementary Table 1. A summary of the time-resolved PL lifetime parameters obtained for the glass, C₆₀, PCBM, PEDOT:PSS, and Spiro-MeOTAD/perovskite systems described in Supplementary Figure

2b. Intensity weighted average lifetime was calculated by $\tau_{avg} = \frac{\sum_i A_i \tau_i^2}{\sum_i A_i \tau_i}$

Bottom Layer		PbI ₂ (12.7°)	MAPbI ₃ (14.2°)
C ₆₀ (ETL)	Before	428	7867
	After	6077	1031
	Ratio	18.38	17.0%
PCBM (ETL)	Before	632	9895
	After	9215	2181
	Ratio	14.58	22.0%
Spiro-MeOTAD (HTL)	Before	651	7599
	After	2614	4612
	Ratio	4.02	60.7%
PEDOT:PSS (HTL)	Before	772	13804
	After	2371	10508
	Ratio	3.07	76.1%

Supplementary Table 2. XRD intensities of the PbI₂ (12.7°) and MAPbI₃ (14.2°) peaks obtained for the perovskite layers deposited on the C₆₀, PCBM, Spiro-MeOTAD, and PEDOT:PSS substrates before and after light exposure.

Electronic Supplementary Information

Decrystallization of CH₃NH₃PbI₃ perovskite crystals via polarity dependent localized charges

Min-cheol Kim^{a†}, Namyoung Ahn^{a†}, Eunhak Lim^b, Young Un Jin^c, Peter V. Pikhitsa^a, Jiyoung Heo^d, Seong Keun Kim^b, Hyun Suk Jung^{c} and Mansoo Choi^{a,e*}*

^aGlobal Frontier Center for Multiscale Energy Systems, Seoul National University, Seoul, Republic of Korea.

^bDepartment of Chemistry, Seoul National University, Seoul, Republic of Korea.

^cSchool of Advanced Materials Science & Engineering, Sungkyunkwan University, Suwon, Gyeonggi-do, Republic of Korea.

^dDepartment of Green Chemical Engineering, Sangmyung University, Seoul, Republic of Korea.

^eDepartment of Mechanical Engineering, Seoul National University, Seoul, Republic of Korea.

[†]These authors contributed equally to this work.

*Correspondence and request for materials should be addressed to H.S.J, and M. C.

(email: hsjung1@skku.edu; mchoi@snu.ac.kr)

To estimate electron and hole densities inside MAPbI₃ layer, the structure is simplified as shown in Supplementary Fig.1. All the layers are ideally uniform along y-direction for building 1D simple model. Thus, we considered carrier densities as a function of thickness displacement along x-direction. Additionally, we assumed that there is no ion migration, no trap-assisted recombination and no photon recycling because those are not dominant under one sun illumination conditions (mainly generation and dynamics of charge carriers). Consequently, we considered light absorption (photo-carrier generation), radiative recombination, carrier diffusion and carrier drift inside MAPbI₃ perovskite layers by utilizing its physical properties according to the references [ref].

First, the carrier transport model is regarded as the following Boltzmann transport equations.

$$J_e = -q\mu_e n_e \nabla \varphi_{F,e} \quad \text{Eq 1}$$

$$J_h = -q\mu_h n_h \nabla \varphi_{F,h} \quad \text{Eq 2}$$

Where q is the elementary charge, μ_e and μ_h are the mobility of electron and hole, n_e and n_h are the density of electron and hole, $\varphi_{F,e}$ and $\varphi_{F,h}$ are the quasi Fermi level of electron and hole, respectively.

The quasi Fermi level is given by

$$\varphi_{F,e} = E_{CB} + V - \frac{kT}{q} \ln \frac{n_e}{N_0} \quad \text{Eq 3}$$

$$\varphi_{F,h} = E_{VB} + V + \frac{kT}{q} \ln \frac{n_h}{N_0} \quad \text{Eq 4}$$

Where E_{cb} and E_{vb} are the energy level of conduction band and valence band, V is the electrostatic potential, k is Boltzmann's constant, T is the temperature, N_0 is the total density

of state

Accordingly, the current density of electrons and holes (J_e and J_h) could be calculated as follows.

$$\therefore J_e = -q\mu_e n_e \left(\frac{dV}{dx} - \frac{kT}{q} \frac{1}{n_e} \frac{dn_e}{dx} \right) = -q\mu_e n_e \frac{dV}{dx} + \mu_e kT \frac{dn_e}{dx}$$

... Eq 5

$$\therefore J_h = -q\mu_h n_h \left(\frac{dV}{dx} + \frac{kT}{q} \frac{1}{n_h} \frac{dn_h}{dx} \right) = -q\mu_h n_h \frac{dV}{dx} - \mu_h kT \frac{dn_h}{dx}$$

... Eq 6

The first term is associated with carrier drift, and the second one is corresponding to carrier diffusion by density difference.

To calculate carrier densities, the continuity equation of carriers is required. Considering carrier generation (G) and carrier recombination (R), the continuity equation of electrons and holes

are expressed as the following equations.

$$\frac{dn_e}{dt} = \frac{1}{q} \frac{dJ_e}{dx} + G - R$$

Eq 7

$$\frac{dn_h}{dt} = -\frac{1}{q} \frac{dJ_h}{dx} + G - R$$

Eq8

Recombination R is calculated by following a Langevin process as expressed in Eq. 9, and generation G is calculated according to the

reference.¹

$$R = L \frac{q(\mu_e + \mu_h)}{\epsilon_0 \epsilon_r} n_e n_h$$

Eq 9

Finally, we can obtain the continuity equation of carrier in the 1D model by using Eq, 5-9, as shown in below.

$$\frac{dn_h}{dt} = -\frac{1}{q} \frac{dJ_h}{dx} + G - R = \mu_h n_h \frac{d^2 V}{dx^2} + \mu_h \frac{dn_h}{dx} \frac{dV}{dx} + \frac{\mu_h kT}{q} \frac{d^2 n_h}{dx^2} - L \frac{q(\mu_e + \mu_h)}{\varepsilon_0 \varepsilon_r} n_e n_h + G$$

Eq 10

$$\frac{dn_e}{dt} = \frac{1}{q} \frac{dJ_e}{dx} + G - R = -\mu_e n_e \frac{d^2 V}{dx^2} - \mu_e \frac{dn_e}{dx} \frac{dV}{dx} + \frac{\mu_e kT}{q} \frac{d^2 n_e}{dx^2} - L \frac{q(\mu_e + \mu_h)}{\varepsilon_0 \varepsilon_r} n_e n_h + G$$

Eq 11

At the steady-state, the time derivative of carrier density is zero ($dn_e/dt=dn_h/dt=0$). Therefore,

Eq 10 and 11 could be simplified more.

$$\frac{\mu_e kT}{q} \frac{d^2 n_e}{dx^2} = \mu_e n_e \frac{d^2 V}{dx^2} + \mu_e \frac{dn_e}{dx} \frac{dV}{dx} + L \frac{q(\mu_e + \mu_h)}{\varepsilon_0 \varepsilon_r} n_e n_h - G$$

Eq

12

$$\frac{\mu_h kT}{q} \frac{d^2 n_h}{dx^2} = -\mu_h n_h \frac{d^2 V}{dx^2} - \mu_h \frac{dn_h}{dx} \frac{dV}{dx} + L \frac{q(\mu_e + \mu_h)}{\varepsilon_0 \varepsilon_r} n_e n_h - G$$

Eq

13

Potential terms can be solved from poisson equation of Gauss law.

$$\nabla^2 V = -\frac{q}{\varepsilon_0 \varepsilon_r} (n_h - n_e)$$

Poisson equation

$$\frac{d^2 V}{dx^2} = -\frac{q}{\varepsilon_0 \varepsilon_r} (n_h - n_e)$$

Poisson equation in 1D model

Finally, the continuity equation of electrons and holes at the steady-state are obtained as a function of electron and hole densities and thickness displacement x as the following equations.

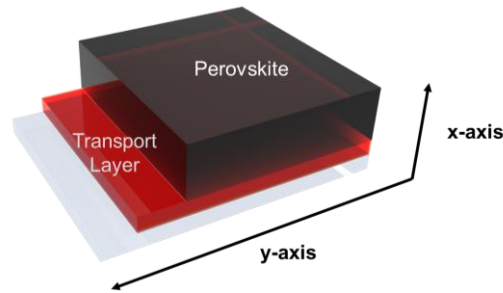
$$\therefore \frac{\mu_e kT}{q} \frac{d^2 n_e}{dx^2} = \frac{q\mu_e}{\varepsilon_0 \varepsilon_r} (n_e^2 - n_e n_h) + \mu_e \frac{dn_e}{dx} \frac{q}{\varepsilon_0 \varepsilon_r} \left(\int (n_e - n_h) dx - E_{x0} \right) + L \frac{q(\mu_e + \mu_h)}{\varepsilon_0 \varepsilon_r} n_e n_h - G$$

Eq 14

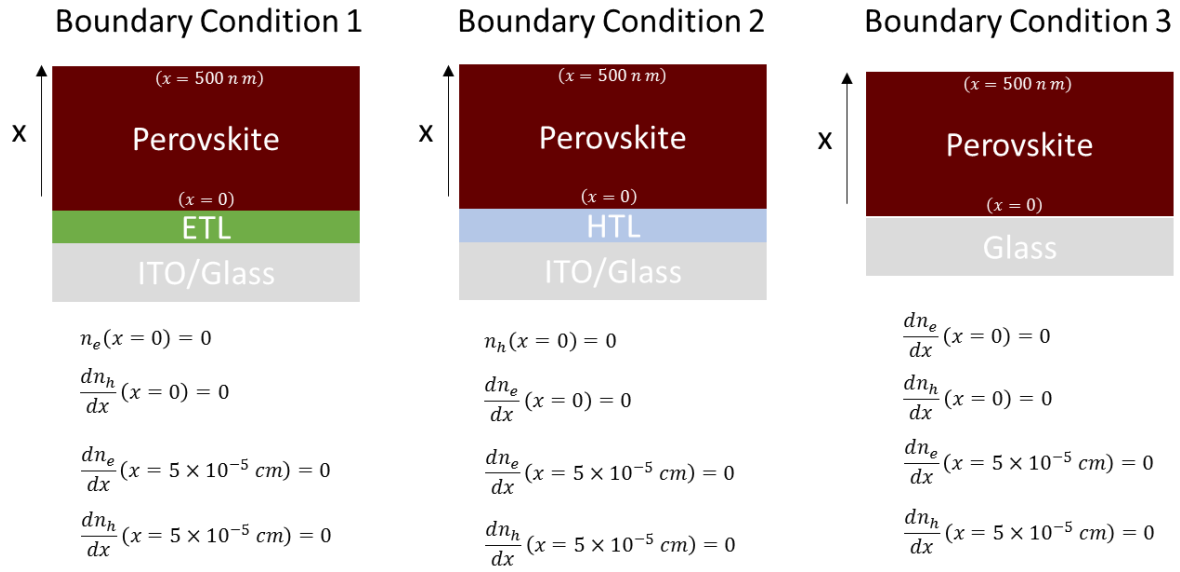
$$\therefore \frac{\mu_h kT}{q} \frac{d^2 n_h}{dx^2} = \frac{q\mu_h}{\varepsilon_0 \varepsilon_r} (n_h^2 - n_e n_h) - \mu_h \frac{dn_h}{dx} \frac{q}{\varepsilon_0 \varepsilon_r} \left(\int (n_e - n_h) dx - E_{x0} \right) + L \frac{q(\mu_e + \mu_h)}{\varepsilon_0 \varepsilon_r} n_e n_h - G$$

Eq 15

To solve equation 14 and 15 for calculating electron and hole densities inside three kinds of half devices, four boundary conditions regarding densities at edges ($x=0$ and 500 nm) are required. At the interface of the electron transport layer, electron density is considered to be zero based on experimental results of PL measurement (Most of carriers are quenched by charge selective layer). On the other hand, hole density is zero at the interface of the hole transport layer. Moreover, since there is no carrier diffusion at the boundary, density difference is regarded to be zero. Finally, we defined boundary conditions for the ETL/MAPbI₃, the HTL/MAPbI₃, and the glass/MAPbI₃ devices as shown in Supplementary Fig 2



Supplementary Information Figure 1. Simplified 1-d model for Transport Layer/Perovskite using in this calculation



Supplementary Information Figure 2. Boundary conditions for ETL/MAPbI₃, the HTL/MAPbI₃, and the glass/MAPbI₃ devices to solve equation 14 and 15.

We could obtain numerical solutions for simultaneous equations 14 and 15 by using MATLAB.

Parameter values for the model are shown in Supplementary Table.1

Parameter	Unit	Value
Q (unit charge)	C	1.6×10^{-19}
μ_e (electron mobility)	$\text{cm}^2\text{V}^{-1}\text{s}^{-1}$	5
μ_h (hole mobility)	$\text{cm}^2\text{V}^{-1}\text{s}^{-1}$	3
k (Boltzmann Constant)	JK^{-1}	1.38×10^{-23}
T (Temperature)	K	300
L (Recombination constant)		10^{-5}
ϵ_0 (Vacuum Permittivity)	$\text{CV}^{-1}\text{cm}^{-1}$	8.854×10^{-10}
ϵ_r (Relative Permittivity)		60
G (Carrier Generation)		1.7×10^{21}
α (absorption coefficient)	cm^{-1}	1.48×10^4

Reference

1. S. van Reenen, M. Kemerink and H. J. Snaith, *The Journal of Physical Chemistry Letters*, 2015, **6**, 3808-3814.